Supplement of Atmos. Chem. Phys., 26, 4917–4936, 2026
https://doi.org/10.5194/acp-26-4917-2026-supplement

Atmospheric Chemistry and Physics
Open Access
EGU

Supplement of

Novel insights on causes of disproportionate trends between particulate NO_3^- and NO_x emissions in Canadian urban atmospheres

Qinchu Fan et al.

Correspondence to: Xiaohong Yao (xhyao@ouc.edu.cn) and Leiming Zhang (leiming.zhang@ec.gc.ca)

S1. A brief review of literature-reported long-term trends in particulate nitrate in response to NO_x emission reductions in Canada, the United States, Europe, and China

Within Canada, long-term observations indicate that trends in inorganic aerosols are neither spatially uniform nor monotonic. For example, in Toronto, both nitrate (NO_3^-) and sulfate (SO_4^{2-}) in $PM_{2.5}$ (particles < 2.5 μm) declined rapidly during 2004–2017 (-6.9% yr^{-1} and -8.1% yr^{-1}, respectively), accompanied by decreases in ammonium (NH_4^+) (Jeong et al., 2020). In contrast, in Edmonton (2007–2014), neither $PM_{2.5}$ nor the major inorganic ions (NO_3^-, SO_4^{2-}, NH_4^+) exhibited statistically significant trends (Bari and Kindzierski, 2016).

At a broader rural and non-urban scale, data collected through the Canadian Air and Precipitation Monitoring network (CAPMoN) (1988–2007) revealed distinct non-monotonic annual variations in particulate NO_3^- in total suspended particles (TSP): approximately stable during 1988–1993, increasing during 1993–2002, and declining during 2002–2007. Site-to-site differences suggest strong modulation by meteorology, long-range transport, and aerosol thermodynamics in addition to precursor emissions (Zbieranowski and Aherne, 2012).

This asymmetry between particulate SO_4^{2-} and NO_3^- responses becomes clearer at the eastern North American scale (Feng et al., 2020). During 1990–2015, SO_2 emissions fell sharply (−84% in the eastern U.S.; −66% in eastern Canada), while NO_x reductions were more modest (−54% and −22%, respectively). Corresponding, SO_4^{2-} and NH_4^+ in TSP decreased substantially (−73.3% and −67.4%), whereas NO_3^- decreased by only −29.1% (largely after 2000), indicating that NO_3^- responds more weakly and more conditionally to emission controls than SO_4^{2-} and NH_4^+.

Winter-focused analyses further illustrate why NO_{3-} can resist or even offset expected declines. Shah et al. (2018) compared winter conditions in 2007 and 2015 and found that, despite substantial reductions in winter SO_2 (-58%) and NO_x (−35%) emissions, winter $PM_{2.5}$ NO_3^- showed little change. Similarly, a detailed analysis at paired urban and rural sites in Rhode Island (northeastern U.S.) reported pronounced increases in NO_3^- in PM_{10} (particle < 10 μm) during 2005–2015 (+95% urban; +57%

rural) despite substantial SO_2 and NO_x emission reductions, consistent with acidity- and partitioning-driven feedbacks that can partially counteract NO_x controls (Kim et al., 2023).

In line with the findings described above, early NO_x-control phases were sometimes accompanied by rising particulate NO_3^- across the eastern U.S. For example, NO_3^- in TSP increased by 11% from 1990–1994 to 2000–2004 (winter: 31%) even as NO_x emissions declined by 22% (Sickles II and Shadwick, 2015). Similarly, at several CAPMoN sites (ALG, LON, EGB, and KEJ) in Canada, NO_3^- in TSP increased significantly during 1993-2002 followed by declines during 2002-2007 (Zbieranowski and Aherne, 2011). These findings underscore the nonlinear and phase-dependent response of nitrate to precursor controls.

Comparable non-linearities have also been documented in other fast-changing regions. In Europe, EMEP assessments report >80% reductions in SO_x and ~50% reductions in NO_x, but only ~12% reductions in NH_3 during 2000–2019. Correspondingly, particulate SO_4^{2-} in TSP declined at ~3–4% yr^{-1}, whereas total nitrate (HNO_{3gas} + particulate NO_3^-) decreased more slowly at ~1.5–2% yr^{-1} (Aas et al., 2024). Observations in the United Kingdom further illustrate phase-dependent decoupling: at two London sites, NO_3^- in PM_{10} changed only slightly during 2012–2018 and became largely stagnant after 2014, despite continued significant declines in ambient NO_x and NO_2; meanwhile, rural AGANET measurements (2000-2020) show that NO_3^- in TSP decreased at 2.12% yr^{-1}, significantly slower than the decline in NO_x emissions (2.84% yr^{-1}) and rural NO_x concentrations (3.48% yr^{-1}), implying an increasing nitrate-to-precursor ratio over time and highlighting the roles of NH_3 availability, thermodynamic partitioning, and regional transport (Harrison et al., 2022).

In contrast, under aggressive SO_2 controls in North China (2008–2016), SO_2, NO_x and NH_3 emissions decreased by −60%, −16% and −7%, respectively (Liu et al., 2018). Nevertheless, $PM_{2.5}$ NO_3^- increased by ~28%, accompanied by a ~30% rise in gas-phase NH_3, underscoring how shifts in aerosol acidity and NH_3 availability can redirect inorganic aerosol composition and even promote nitrate under certain control phases (Liu et al., 2018).

The cross-regional comparisons presented in this section underscore the inherently nonlinear behavior of particulate nitrate trends. This complexity calls for a regionally focused Canadian synthesis that explicitly accounts for the coupled evolution of SO_2, NO_x, and NH_3 emissions, thermodynamic partitioning processes, and meteorological variability when interpreting long-term f-NO_3^- trends.

S2. Analysis of the relative importance of 15 major variables on f-NO_3^- formation using a Random Forest model

The Random Forest (RF) model embedded in the *"ranger"* R package was used here to simulate the nonlinear relationship between daily f-NO_3^- and a suite of 15 predictor variables (Schmid et al., 2016; Wright and Ziegler, 2017). These predictors include NO_2 and $PM_{2.5}$ concentrations; near-surface meteorological variables including wind speed and direction (WS, WD), relative humidity (RH), temperature (T), dew point, visibility, and surface pressure; boundary-layer height (BLH); surface shortwave radiation (SSR); total cloud cover (TCC); total precipitation (TP); and two seasonal timing variables. The two seasonal timing variables was encoded with two Fourier terms—sin and cos of day-of-year (DOY)—to capture the annual cycle without year-end discontinuity.

Hourly WS, WD, RH, T, surface pressure, dew point, and visibility were obtained from the Edmonton International Airport station via *"worldMet"* R package and aggregated to daily means. Daily BLH, SSR, TCC, and TP were sourced from ERA5 (Copernicus Climate Data Store) and harmonized to time zone-specific daily values. The model was trained using a randomly selected 70% subset of data from 2010–2019, with the remaining 30% data reserved for model performance evaluation (Fig. S8a). Sensitivity tests indicated that selecting 1,000 trees with a minimum node size of 6 provided stable performance.

For the 30% test data set, the ordinary-least-squares slope of predicted versus observed values was 0.54, with MSE = 1.2 μg m^{-3}, MAE = 0.42 μg m^{-3}, and R^2 = 0.68. Permutation-based variable importance (Fig. S8b) ranked predictors in ascending order of importance from top to bottom. Temperature emerged as the most influential variable (Importance ≈ 0.114), followed by $PM_{2.5}$ (0.064), NO_2 (0.061), and BLH (0.052).

Moisture metrics (dew point 0.037; RH 0.013) and SSR (0.021) were moderately informative. Transport- and optics-related variables also contribute to some extent (WD, 0.013; WS, 0.007; visibility, 0.011), though less strongly than the leading predictors mentioned above. In contrast, cloud, precipitation, and pressure played minimum role on the daily scale (TCC, 0.003; TP, 0.002; pressure, 0.002).

Partial dependence plots for the top three predictors identified by permutation importance (T, $PM_{2.5}$, and NO_2) (Fig. S8c–e) show a strong non-linear relationship between predicted f-NO_3^- and temperature, characterized by a sharp decline around 0°C. In contrast, $PM_{2.5}$ and NO_2 display threshold-like increases followed by saturation, suggesting that cold conditions strongly favor particulate nitrate persistence, whereas the impacts of pollution intensity and NO_x-related indicators are modulated and ultimately constrained by other limiting factors.

S3. Simulation of secondary f-NO_3^- formation using the Flexible 0-D Atmospheric Model (F0AM)

The Flexible 0-D Atmospheric Model (F0AM) with the CB6r2 chemical mechanism was used to simulate f-NO_3^- formation on ten days with f-NO_3^- concentration higher than 9 μg m^{-3} in 2010 (00:00–23:00 local time), results from which can quantify the maximum retainable secondary f-NO_3^- (Luecken et al., 2019; Wolfe et al., 2016). Simulations were run in MATLAB with a 1-h external step (adaptive internal sub-stepping) and full time-series output. The box model was constrained by the observed NO_2, O_3, and CO; all other species evolved freely. To avoid numerical instability, initial conditions were set to NO = 10^{-4} ppb and HNO_3 = 10^{-3} ppb. Meteorological inputs including surface pressure (P), temperature (T), relative humidity (RH), and solar zenith angle (SZA) were computed from site latitude/longitude and local time. Surface albedo was fixed at 0.1. Photolysis frequencies followed F0AM's SZA-driven parameterization using a TOMS-like total O_3 column from OMI/Aura Level-3 (OMTO3d, 1°×1°) retrieved via NASA GES DISC Giovanni and interpolated to the model time resolution. The dilution constant k_{dil} was inferred from CO as a quasi-conservative tracer. HNO_3 dry deposition was represented as $k_{dep}=(v_d/100)/H$, where v_d

is the dry-deposition velocity (cm s^{-1}) and H is the boundary-layer height (m).

From model reaction rates we diagnosed total gas-phase HNO_3 production P_{gas} and the OH + NO_2 → HNO_3 channel P_{OH}. Nighttime heterogeneous N_2O_5 hydrolysis was included as a diagnostic upper bound and applied only when SZA > 90°:

$$P_{N_2O_5}^{het} = Yk_{het}[N_2O_5] \quad \text{(S1)}$$

$$k_{het} = \frac{\gamma \bar{c} S_A}{4} \quad \text{(S2)}$$

where Y is the stoichiometric HNO_3 yield per N_2O_5 uptake, γ is the uptake coefficient of N_2O_5 (removal probability of N_2O_5 per collision with the wet aerosol surface), $\bar{c}$ is the mean molecular speed of N_2O_5, and S_A is the aerosol surface area concentration.

Over each 24-h window we integrated total chemical production and diagnostic losses:

$$P_{chem} = \int (P_{gas} + P_{N_2O_5}^{het}) dt \quad \text{(S3)}$$

$$P_{loss} = \int (k_{dil}[HNO_3]^+ + k_{dep}[HNO_3]) dt \quad \text{(S4)}$$

where P_{gas} is the total gas-phase HNO_3 production rate (ppb s^{-1}), and $[HNO_3]^+$ = max ($[HNO_3] - [HNO_3]_{bkg}$, 0) with $[HNO_3]_{bkg}$ = 0 to provide a local-increment upper bound. The retainable upper bound of secondary particulate nitrate was then calculated as:

$$NO_{3\,sec,max}^- = \alpha \max(P_{chem} - P_{loss}, 0) \quad \text{(S5)}$$

where α converts ppb to μg m^{-3} for nitrate using the daily mean T and P. To avoid double counting, $P_{N_2O_5}^{het}$ (Eq. S1) was added only if the gas-phase mechanism lacked an explicit N_2O_5→HNO_3 pathway.

In a baseline configuration designed to represent a typical mid-latitude winter urban setting (γ = 0.01, S_A=200 , Y=1.5; Mielke et al., 2016; Zang et al., 2022), the retainable secondary particulate nitrate was 2.5 μg m^{-3} on January 19, 2010 (the highest observed f-NO_3^- in 2010) and 0.3 μg m^{-3} on December 7, 2010 (the second highest observed f-NO_3^- in 2010) , corresponding to 14% and 1.4% of observed f-NO_3^-, respectively (Table S2a). Using empirical estimates of aerosol surface area derived

from $PM_{2.5}$ with RH growth and T (S_A=583 and 554 for 2010-01-29 and 2010-12-07; γ held at 0.01), the retainable secondary burden increased to 4.4 and 6.7 μg m^{-3}, i.e., 25% and 39%, respectively, of the observed values (Table S2b). The latter parameters, however, resulted in the predicted f-NO_3^- to as high as 86 μg m^{-3} on February 28, 2010, which were six times of the observed value and is practically impossible in Canada. Thus, all predicted values larger than the observations were excluded for further analysis.

When examining the well-behaved simulation cases in Table S2ab, all predicated values were substantially smaller than the observations, except for 1 December 2010 (S_A=338 and γ at 0.015). Even in the empirical-estimate cases, where predictions are generally larger, the contribution of retainable secondary particulate nitrate never exceeds 45% of the observed f-NO_3^-. Overall, the test results suggested that the primary f-NO_3^- dominantly contributed to the higher values of f-NO_3^- in winter.

S4. Description of the hypothesis: Was the observed f-NO_3^- entirely derived from the condensation of HNO_{3gas}* in Canadian urban atmospheres during the cold season?

To test the hypothesis if the observed f-NO_3^- was entirely derived from the condensation of HNO_{3gas}* (≈HNO_{3gas} + N_2O_{5gas}) in Canadian urban atmospheres during the cold season, we first analyzed the 20 daily samples in 2010 with f-NO_3^- concentration of > 4 μg m^{-3} (out of 116 total samples that year). For these 20 samples, the mass ratios of f-NO_3^- to HNO_{3gas} varied from 21 to >100, with a median value of 63.

Assuming that the observed f-NO_3^- was entirely derived from the condensation of HNO_{3gas}* (≈HNO_{3gas} + N_2O_{5gas}), mass conservation requires that the net production of f-NO_3^- equal the net loss of HNO_{3gas}^*. Because the observed concentrations of f-NO_3^- were one to two orders of magnitude higher than those of HNO_{3gas}^*, this hypothesis implicitly requires a quasi-static condition for HNO_{3gas}^* (i.e., $d[HNO_{3gas}^*]/dt \approx 0$). Such a condition would imply that the rapid formation of HNO_{3gas}^* is balanced by its removal through conversion into f-NO_3^-. Similar quasi-static approximations are commonly applied in the literature to infer concentrations of highly reactive species (e.g., OH radicals).

However, the daily time resolution of our dataset does not permit direct estimation of f-NO_3^- formation rates. Therefore, we evaluated the hypothesis indirectly. If the condition $d[HNO_{3gas}^*]/dt \approx 0$ accompanied with the balanced rapid formation and removal of HNO_{3gas}^* does not hold for the 20 samples, the above hypothesis fails. If the removal rate of HNO_{3gas}^* approaches zero while its formation remains rapid, the concentration of HNO_{3gas}^* would be expected to increase substantially. Under such circumstances, low concentrations of f-NO_3^- should be associated with a low removal rate of HNO_{3gas}^* in the process of f-NO_3^- formation. Thus, the examination of $d[HNO_{3gas}^*]/dt \approx 0$ accompanied with the balanced rapid formation and removal of HNO_{3gas}^* is further reframed into testing a weaker hypothesis: whether HNO_{3gas}^* concentrations significantly increased under conditions with low f-NO_3^- concentrations, compared to cases with high f-NO_3^- concentrations. Such an increase would be necessary, but not sufficient to accept the quasi-static approximation. Conversely, if no such increase was observed, the hypothesis must be rejected, i.e., the observed low concentrations of HNO_{3gas}^* could not have given rise to high f-NO_3^- concentrations prior to their detection at the sampling site, based on the principle of mass conservation.

S5. A brief review of the overall performance of particulate nitrate modeling in Canada and the United States.

S5.1. Overall model performance and the "error compensation" challenge in simulating particulate nitrate

Chemical transport models (CTMs; e.g., AURAMS, CMAQ, GEOS-Chem, and GEM-MACH) have been widely used to simulate particulate nitrate (NO_3^-) and generally reproduce the broad spatial patterns and key controlling processes across Canada and the U.S. However, they frequently exhibit systematic biases in concentration magnitude, long-term trends, and sensitivities to emission controls, along with a substantial risk of "error compensation" (ECCC, 2016; Kim et al., 2014, 2023; Luo et al., 2019; Pappin et al., 2024; Pun et al., 2009; Russell et al., 2019; Semeniuk et al., 2025; Shah et al., 2018; Smyth et al., 2009; Walker et al., 2012).

Multi-model evaluations highlight pronounced regional heterogeneity in model errors and the potential of an "illusion of good agreement" in total PM mass. For example, the standard GEOS-Chem v12.0.0 simulation substantially overestimated surface $PM_{2.5}$ NO_3^- over the U.S. (1.89 μg m^{-3} vs. 0.70 μg m^{-3}), with strong spatial heterogeneity: outside California the normalized mean bias (NMB) reached +176%, whereas California showed an opposite bias (−62%), implying region-dependent dominant error sources (meteorology, emissions, or thermodynamics) (Luo et al., 2019; Walker et al., 2012). Even in high-resolution simulations for California's San Joaquin Valley (CMAQ-MADRID), $PM_{2.5}$ NO_3^- was overestimated by 35%, indicating that uncertainties in emissions and gas–particle partitioning can be amplified under local conditions (Pun et al., 2009).

Cross-model comparisons further demonstrate that "getting PM mass right" does not guarantee correct composition: although both AURAMS and CMAQ v4.6 underestimated total $PM_{2.5}$ in July 2002, CMAQ performed better for the nitrate component than AURAMS, suggesting that different models may achieve similar total mass through compensating errors among individual components (Smyth et al., 2009).

Importantly, condensable particulate NO_3^-, as defined by the Environmental Protection Agency (2017), as well as its enhanced fraction under freezing ambient conditions, remains absent from current emission inventories. Incorporating this component could be critical for improving the performance of particulate NO_3^- simulations, particularly during cold winter seasons across Canada and the northern United States.

S5.2. Imbalance in regional research depth: intensive mechanism-based studies in the U.S. versus limited Canada-focused assessments

A notable gap lies in the uneven depth of regional investigation. In the U.S., numerous studies have conducted systematic, quantitative evaluations and mechanistic decomposition of particulate NO_3^-. In some of these studies, CTM simulations relevant to Canada treat the country within a broader North American or primarily as part of transboundary analyses. In contrast, relatively few stand-alone, Canada-focused

assessments provide detailed quantitative attribution and process-level evaluation (ECCC, 2016; Pappin et al., 2024).

Existing modeling efforts over the Canadian domain generally fall into three categories, each reflecting the broader CTM challenges noted above:

(1) Operational model development: Advancements in Canada's operational CTM (GEM-MACH), including updates such as incorporation of the MOSAIC aerosol module, demonstrate that particulate NO_3^- is highly sensitive to dry deposition parameterizations. Earlier model configurations also lacked key processes (e.g., heterogeneous hydrolysis of N_2O_5), limiting performance in simulating wintertime particulate NO_3^- (Semeniuk et al., 2025).

(2) High-resolution simulations over major source regions: Nested, high-resolution simulations targeting industrial hotspots (e.g., oil sands regions) indicate that finer spatial resolution improves representation of plume peaks. However, conventional site-based evaluation metrics may be "masked" by small wind-direction biases and uncertainties in emission spatial allocation, complicating interpretation of localized chemical processes (Russell et al., 2019).

(3) Uncertainty in transboundary attribution: Studies quantifying the contribution of U.S. emissions to Canada's $PM_{2.5}$-related health burden emphasize that chemical nonlinearity, particularly for NO_3^-, can substantially amplify uncertainties in scenario-based approaches (e.g., zero-out methods) (Pappin et al., 2024).

S5.3. Key mechanism constraints: removal processes, heterogeneous chemistry, and thermodynamics

Across both Canada and the U.S., accurately representing physical removal and chemical formation pathways is essential for simulating particulate NO_3^-. On the physical side, improved wet-scavenging parameterizations, such as incorporating time-varying in-cloud condensate and scavenging rates, can substantially enhance model performance. In GEOS-Chem, for example, such updates reduced the annual mean simulated particulate NO_3^- in the U.S. from 1.89 to 0.88 $\mu g\ m^{-3}$, underscoring that wet

removal can constrain fine NH_4NO_3 as strongly as chemical production does (Luo et al., 2019).

Mechanistically, wintertime particulate NO_3^- is highly sensitive to nocturnal heterogeneous chemistry. Process-level diagnostics indicate that winter production of particulate NO_3^- in the U.S. Midwest is dominated by heterogeneous N_2O_5 conversion (~57%), followed by OH + NO_2 reactions (~28%) (Kim et al., 2014). In rural California, approximately two-thirds of particulate NO_3^- formation is likewise attributed to heterogeneous pathways (Pun et al., 2009).

Importantly, particulate NO_3^- responds to NO_x controls in a strongly nonlinear manner and may even exhibit counterintuitive trends, posing a persistent "acidity–partitioning" challenge for long-term simulations. Between 2005 and 2015 in the northeastern U.S., PM_{10} nitrate increased by 95% in urban areas and 57% in rural areas despite declining NO_x emissions; modeling attributed this pattern to shifts in aerosol acidity and gas–particle partitioning that offset the expected benefits of precursor reductions (Kim et al., 2023). Analyses using GEOS-Chem further suggest that substantial SO_2 reductions from 2007 to 2015 decreased aerosol acidity (i.e., increased pH), thereby favoring partitioning of HNO_3 into the particle phase and diminishing the marginal effectiveness of NO_x controls for reducing particulate NO_3^- (Shah et al., 2018).

This thermodynamic feedback also helps explain why chemical transport models may underestimate observed nitrate declines. For example, CMAQ simulated much weaker decreases (−0.4% to −0.5% yr^{-1}) than those observed (−2.1% to −2.5% yr^{-1}) and failed to capture interannual variability (Xing et al., 2015). Over a 25-year period, total inorganic nitrate (TNO_3) declined by 52.6%, whereas particulate NO_3^- decreased by only 29.1%, further demonstrating a delayed and conditional response governed by evolving neutralization efficiency and partitioning dynamics (Feng et al., 2020).

S5.4. Summary and implications

Overall, uncertainties in model simulated particulate NO_3^- are governed by three primary factors: (1) emission inventories**,** particularly biases in NH_3 and NO_x that propagate through both chemical production and deposition pathways; (2) key chemical

and thermodynamic parameters, including $\gamma(N_2O_5)$ and aerosol pH sensitivity; and (3) physical processes and model resolution, such as simplified wet-removal schemes and biases in nighttime boundary-layer height.

Future research should move beyond simply "matching $PM_{2.5}$ mass" and instead adopt a multi-constraint framework that jointly evaluates particle size distributions, acidity–partitioning diagnostics (e.g., pH and TNO_3), heterogeneous chemistry (e.g., N_2O_5 uptake), and seasonal NH_3 variability. In particular, sensitivity analyses should explicitly identify the conditions under which NO_x controls become less effective due to acidity-driven partitioning shifts. Doing so would elevate nitrate trend attribution and health-benefit assessments from empirical model fitting to mechanistically testable science.

Notably, condensable particulate NO_3^-, as defined by the Environmental Protection Agency (2017), and its enhanced fraction under freezing ambient conditions are not currently included in emission inventories. Given their demonstrated importance in this study, these components should be urgently incorporated into inventories to improve the accuracy of f-NO_3^- predictions in 3-D air quality models.

References

Aas, W., Mortier, A., Bowersox, V., Cherian, R., Faluvegi, G., Fagerli, H., Hand, J., Klimont, Z., Galy-Lacaux, C., Lehmann, C. M. B., Myhre, C. L., Myhre, G., Olivié, D., Sato, K., Quaas, J., Rao, P. S. P., Schulz, M., Shindell, D., Skeie, R. B., Stein, A., Takemura, T., Tsyro, S., Vet, R., and Xu, X.: Global and regional trends of atmospheric sulfur, Sci. Rep., 9, 953, https://doi.org/10.1038/s41598-018-37304-0, 2019.

Bari, M. A. and Kindzierski, W. B.: Eight-year (2007–2014) trends in ambient fine particulate matter ($PM_{2.5}$) and its chemical components in the capital region of Alberta, Canada, Environ. Int., 91, 122–132, https://doi.org/10.1016/j.envint.2016.02.033, 2016.

ECCC: Canada–United States transboundary particulate matter science assessment 2013, https://publications.gc.ca/site/eng/9.811711/publication.html, last access: 13 November 2025, 2016.

Environmental Protection Agency: Method 202—Dry Impinger Method for Determining Condensable Particulate Emissions From Stationary Sources, proposed rule, Fed. Regist., 82, 42508–42530, 2017.

Feng, J., Chan, E., and Vet, R.: Air quality in the eastern United States and Eastern Canada for 1990–2015: 25 years of change in response to emission reductions of SO_2 and NO_x in the region, Atmos. Chem. Phys., 20, 3107–3134, https://doi.org/10.5194/acp-20-3107-2020, 2020.

Harrison, R. M., Beddows, D. C. S., Tong, C., and Damayanti, S.: Non-linearity of secondary pollutant

formation estimated from emissions data and measured precursor-secondary pollutant relationships, npj Clim. Atmos. Sci., 5, 71, https://doi.org/10.1038/s41612-022-00297-9, 2022.

Jeong, C.-H., Traub, A., Huang, A., Hilker, N., Wang, J. M., Herod, D., Dabek-Zlotorzynska, E., Celo, V., and Evans, G. J.: Long-term analysis of $PM_{2.5}$ from 2004 to 2017 in Toronto: composition, sources, and oxidative potential, Environ. Pollut., 263, 114652, https://doi.org/10.1016/j.envpol.2020.114652, 2020.

Kim, H., Walters, W. W., Kysela, L., and Hastings, M. G.: Long-term trends in inorganic aerosol chemical composition and chemistry at an urban and rural site in the Northeastern US, Sci. Total Environ., 904, 166848, https://doi.org/10.1016/j.scitotenv.2023.166848, 2023.

Kim, Y. J., Spak, S. N., Carmichael, G. R., Riemer, N., and Stanier, C. O.: Modeled aerosol nitrate formation pathways during wintertime in the Great Lakes region of North America, J. Geophys. Res.-Atmos., 119, 12420–12445, https://doi.org/10.1002/2014JD022320, 2014.

Liu, M., Huang, X., Song, Y., Xu, T., Wang, S., Wu, Z., Hu, M., Zhang, L., Zhang, Q., Pan, Y., Liu, X., and Zhu, T.: Rapid SO_2 emission reductions significantly increase tropospheric ammonia concentrations over the North China Plain, Atmos. Chem. Phys., 18, 17933–17943, https://doi.org/10.5194/acp-18-17933-2018, 2018.

Luecken, D. J., Yarwood, G., and Hutzell, W. T.: Multipollutant modeling of ozone, reactive nitrogen and HAPs across the continental US with CMAQ-CB6, Atmos. Environ., 201, 62–72, https://doi.org/10.1016/j.atmosenv.2018.11.060, 2019.

Luo, G., Yu, F., and Schwab, J.: Revised treatment of wet scavenging processes dramatically improves GEOS-Chem 12.0.0 simulations of surface nitric acid, nitrate, and ammonium over the United States, Geosci. Model Dev., 12, 3439–3447, https://doi.org/10.5194/gmd-12-3439-2019, 2019.

Mielke, L. H., Furgeson, A., Odame-Ankrah, C. A., and Osthoff, H. D.: Ubiquity of ClNO2 in the urban boundary layer of Calgary, Alberta, Canada, Can. J. Chem., 94, 414–423, https://doi.org/10.1139/cjc-2015-0426, 2016.

Pappin, A. J., Charman, N., Egyed, M., Blagden, P., Duhamel, A., Miville, J., Popadic, I., Manseau, P. M., Marcotte, G., Mashayekhi, R., Racine, J., Rittmaster, R., Edwards, B., Kipusi, W., and Smith-Doiron, M.: Attribution of fine particulate matter and ozone health impacts in Canada to domestic and US emission sources, Sci. Total Environ., 909, 168529, https://doi.org/10.1016/j.scitotenv.2023.168529, 2024.

Pun, B. K., Balmori, R. T. F., and Seigneur, C.: Modeling wintertime particulate matter formation in central California, Atmos. Environ., 43, 402–409, https://doi.org/10.1016/j.atmosenv.2008.08.040, 2009.

Russell, M., Hakami, A., Makar, P. A., Akingunola, A., Zhang, J., Moran, M. D., and Zheng, Q.: An evaluation of the efficacy of very high resolution air-quality modelling over the Athabasca oil sands region, Alberta, Canada, Atmos. Chem. Phys., 19, 4393–4417, https://doi.org/10.5194/acp-19-4393-2019, 2019.

Schmid, M., Wright, M. N., and Ziegler, A.: On the use of Harrell's C for clinical risk prediction via random survival forests, Expert Syst. Appl., 63, 450–459, https://doi.org/10.1016/j.eswa.2016.07.018, 2016.

Semeniuk, K., Dastoor, A., and Lupu, A.: Implementation of the MOSAIC aerosol module (v1.0) in the Canadian air quality model GEM-MACH (v3.1), Geosci. Model Dev., 18, 6479–6515, https://doi.org/10.5194/gmd-18-6479-2025, 2025.

Shah, V., Jaeglé, L., Thornton, J. A., Lopez-Hilfiker, F. D., Lee, B. H., Schroder, J. C., Campuzano-Jost, P., Jimenez, J. L., Guo, H., Sullivan, A. P., Weber, R. J., Green, J. R., Fiddler, M. N., Bililign, S., Campos, T. L., Stell, M., Weinheimer, A. J., Montzka, D. D., and Brown, S. S.: Chemical feedbacks weaken the wintertime response of particulate sulfate and nitrate to emissions reductions over the eastern United States, Proc. Natl. Acad. Sci. USA, 115, 8110–8115, https://doi.org/10.1073/pnas.1803295115, 2018.

Sickles II, J. E. and Shadwick, D. S.: Air quality and atmospheric deposition in the eastern US: 20 years of change, Atmos. Chem. Phys., 15, 173–197, https://doi.org/10.5194/acp-15-173-2015, 2015.

Smyth, S. C., Jiang, W., Roth, H., Moran, M. D., Makar, P. A., Yang, F., Bouchet, V. S., and Landry, H.: A comparative performance evaluation of the AURAMS and CMAQ air-quality modelling systems, Atmos. Environ., 43, 1059–1070, https://doi.org/10.1016/j.atmosenv.2008.11.027, 2009.

Walker, J. M., Philip, S., Martin, R. V., and Seinfeld, J. H.: Simulation of nitrate, sulfate, and ammonium aerosols over the United States, Atmos. Chem. Phys., 12, 11213–11227, https://doi.org/10.5194/acp-12-11213-2012, 2012.

Wolfe, G. M., Marvin, M. R., Roberts, S. J., Travis, K. R., and Liao, J.: The framework for 0-D atmospheric modeling (F0AM) v3.1, Geosci. Model Dev., 9, 3309–3319, https://doi.org/10.5194/gmd-9-3309-2016, 2016.

Wright, M. N. and Ziegler, A.: ranger: A fast implementation of random forests for high dimensional data in C++ and R, J. Stat. Softw., 77, 1–17, https://doi.org/10.18637/jss.v077.i01, 2017.

Xing, J., Mathur, R., Pleim, J., Hogrefe, C., Gan, C.-M., Wong, D. C., Wei, C., Gilliam, R., and Pouliot, G.: Observations and modeling of air quality trends over 1990–2010 across the Northern Hemisphere: China, the United States and Europe, Atmos. Chem. Phys., 15, 2723–2747, https://doi.org/10.5194/acp-15-2723-2015, 2015.

Zang, H., Zhao, Y., Huo, J., Zhao, Q., Fu, Q., Duan, Y., Shao, J., Huang, C., An, J., Xue, L., Li, Z., Li, C., and Xiao, H.: High atmospheric oxidation capacity drives wintertime nitrate pollution in the eastern Yangtze River Delta of China, Atmos. Chem. Phys., 22, 4355–4374, https://doi.org/10.5194/acp-22-4355-2022, 2022.

Zbieranowski, A. L. and Aherne, J.: Long-term trends in atmospheric reactive nitrogen across Canada: 1988–2007, Atmos. Environ., 45, 5853–5862, https://doi.org/10.1016/j.atmosenv.2011.06.080, 2011.

Zbieranowski, A. L. and Aherne, J.: Spatial and temporal concentration of ambient atmospheric ammonia in southern Ontario, Canada, Atmos. Environ., 62, 441–450, https://doi.org/10.1016/j.atmosenv.2012.08.041, 2012.

Table S1. Information on pollutant concentrations, meteorological variables, and emissions datasets for each Canadian site.

City (Site)	Variable	Time span (Time resolution)
Edmonton (S-90132)	f-NO_3^- (μg m^{-3})	2007-2019 (with 2014 missing, 3-day)
	f-SO_4^{2-} (μg m^{-3})	2007-2019 (with 2014 missing, 3-day)
	f-NH_4^+ (μg m^{-3})	2007-2019 (with 2014 missing, 3-day)
	$PM_{2.5}$ (μg m^{-3})	2010-2014 (1-hr)
Edmonton (S-90130)	f-NO_3^- (μg m^{-3})	1990-2005 (with 1997 and 1999 missing, 6-day)
	c-NO_3^- (μg m^{-3})	1990-2005 (with 1997 and 1999 missing, 6-day)
	f-SO_4^{2-} (μg m^{-3})	1990-2005 (with 1997 and 1999 missing, 6-day)
	f-NH_4^+ (μg m^{-3})	1992-2005 (with 1997 and 1999 missing, 6-day)
	NO_2 mixing ratio (ppb)	1994-2019 (1-hr)
	$PM_{2.5}$ concentration (μg m^{-3})	2011-2014 (1-hr)
	HNO_{3gas} (μg m^{-3})	2010, 2015 (1-day)
	NO_x emissions (*10^3 tones)	1990-2019 (1-yr)
	SO_2 emissions (*10^3 tones)	1990-2019 (1-yr)
	NH_3 emissions (*10^3 tones)	1990-2019 (1-yr)
	T (℃)	2010, 2015 (1-day)
	WS (m s^{-1})	2010, 2015 (1-day)
	RH (%)	2010, 2015 (1-day)
Winnipeg	f-NO_3^- (μg m^{-3})	1990-2018 (with 1998, 2000, 2005, 2009, 2013, 2014 missing, 6-day)
	c-NO_3^- (μg m^{-3})	1990-2012 (with 1998, 2000, 2005, 2009 missing,6-day)
	NO_2 mixing ratio (ppb)	1990-2019 (1-hr)
	NO_x emissions (*10^3 tones)	1990-2018 (1-yr)
Quebec City	f-NO_3^- (μg m^{-3})	1995-2018 (with 1997, 2000, 2002, 2004, 2005, 2008 missing, 6-day)
	c-NO_3^- (μg m^{-3})	1995-2018 (with 1997, 2000, 2002, 2004, 2005, 2008 missing, 6-day)
	NO_2 mixing ratio (ppb)	1996-2019 (1-hr)
	NO_x emissions (*10^3 tones)	1995-2019 (1-yr)
Montreal	f-NO_3^- (μg m^{-3})	1997-2018 (with 2004, 2005, 2015, and 2016 missing, 6-day)
	c-NO_3^- (μg m^{-3})	1997-2014 (with 2004 and 2005 missing, 6-day)
	NO_2 mixing ratio (ppb)	1996-2019 (1-hr)
Hamilton	f-NO_3^- (μg m^{-3})	1995-2019 (with 2003, 2004, and 2011 missing, 3-day)
	c-NO_3^- (μg m^{-3})	1998-2012 (with 2003, 2004, and 2011 missing, 3-day)
	NO_2 mixing ratio (ppb)	1996-2019 (1-hr)
	NO_x emissions (*10^3 tones)	1995-2019 (1-yr)
Victoria	f-NO_3^- (μg m^{-3})	1990-2018 (with 1991, 1992, 1997, 1998, 2004, 2005, 2009, and 2016 missing, 6-day)
	c-NO_3^- (μg m^{-3})	1990-2012 (with 1991, 1992, 1997, 1998, 2004, 2005, 2009, and 2010 missing, 6-day)
	NO_2 mixing ratio (ppb)	1993-2019 (1-hr)
	NO_x emissions (*10^3 tones)	1990-2019 (1-yr)
Vancouver	f-NO_3^- (μg m^{-3})	1990-2018 (with 1992, 1994, 1999, 2003, 2005, and 2012-2014 missing, 6-day)
	c-NO_3^- (μg m^{-3})	1990-2012 (with 1992, 1994, 1999, 2003, 2005, and 2012-2014 missing, 6-day)
	NO_2 mixing ratio (ppb)	1990-2019 (1-hr)

Table S2. Sensitivity of the retainable upper bound secondary f-NO_3^- (f-$NO_{3\ sec,\ max}^-$) to the uptake coefficient of N_2O_5 (γ) and aerosol surface area concentration (S_A) on ten days in 2010 with f-NO_3^- concentration > 9 μg m^{-3}, evaluated with the F0AM box model.

Date	f-$NO_{3\ obs}^-$ (μg m^{-3})	γ	S_A (μm^2 cm^{-3})	P_{chem} (ppb)	P_{OH} (ppb)	$P_{N_2O_5}$ (ppb)	P_{loss} (ppb)	f-$NO_{3\ sec,\ max}^-$ (μg m^{-3})
2010/01/29	18	0.010	200	2	0.3	2	1	2
2010/12/07	17	0.010	200	1	0.2	0.8	1	0.3
2010/12/25	13	0.010	200	3	0.3	2	2	2
2010/02/25	11	0.010	200	3	1	2	8	0
2010/03/03	9	0.010	200	13	2	11	14	0
2010/01/08	9	0.010	200	1	0.2	0.9	1	0
2010/02/28	14	0.010	200	33	2	30	18	43
2010/02/01	13	0.010	200	13	0.6	13	8	14
2010/01/17	12	0.010	200	27	0.7	25	4	64
2010/12/01	10	0.010	200	7	0.3	7.0	2	15
2010/01/29	18	0.01	583	3	0.3	2	1	4
2010/12/07	17	0.01	554	3	0.2	3	1	7
2010/12/25	13	0.015	478	4	0.3	4	2	5
2010/01/17	12	0.01	95	6	0.7	4	4	5
2010/12/01	10	0.015	338	5	0.3	5	2	8
2010/01/08	9	0.01	182	1	0.2	0.8	1	0
2010/02/28	14	0.015	558	48	2	46	18	86
2010/02/01	13	0.01	360	16	0.6	15	8	22
2010/02/25	11	0.015	513	16	1	14	8	23
2010/03/03	9	0.015	513	13	2	11	10	10

- f-$NO_{3\ obs}^-$, the observed f- NO_3^- concentration; P_{chem}, total chemical production of f-NO_3^-; P_{OH}, production of f-NO_3^- via $OH+NO_2 \rightarrow HNO_3$; $P_{N_2O_5}$, production of f-NO_3^- by nighttime heterogeneous N_2O_5 hydrolysis; P_{loss}, losses of f-NO_3^- via dilution and dry deposition.
- The top block reports day-specific γ and S_A estimates and the bottom block shows a baseline representative of a mid-latitude winter urban setting (γ = 0.01, S_A=200).

Cells highlighted in orange indicate cases where f-$NO_{3\ sec,\ max}^-$ exceeds f-$NO_{3\ obs}^-$.

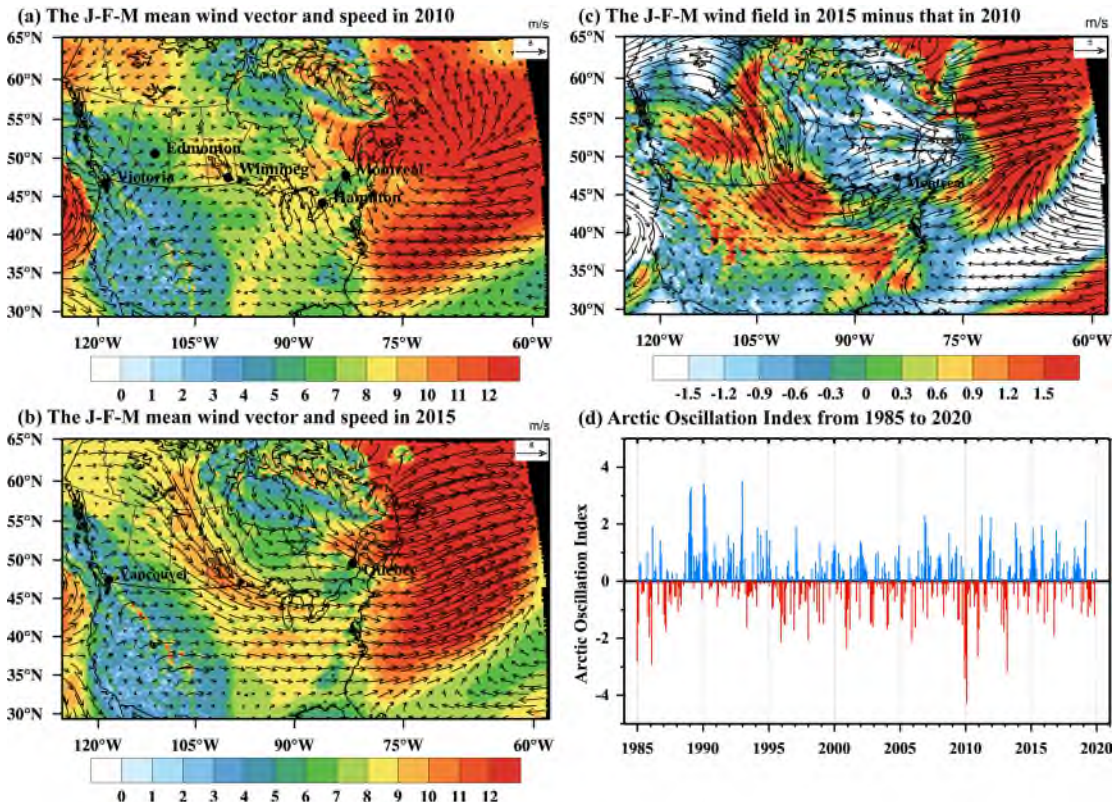

Figure S1. Mean wind vector in January-February-March (JFM) in 2010 (a) and 2015 (b), the difference in the JFM mean wind vector between 2010 and 2015 (2015 minus 2010) (c), and Arctic Oscillation Index from 1990 to 2020 (d)

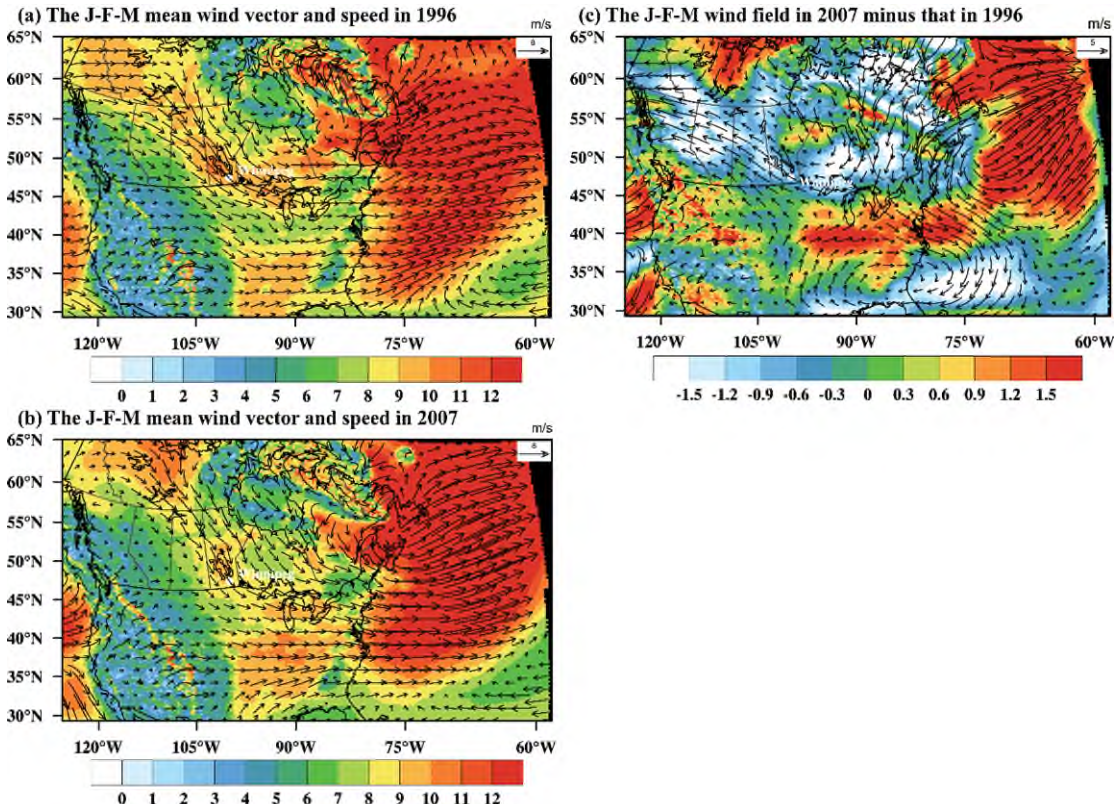

Figure S2. Same as in Figure S1a-c except for 1996 (a) and 2007 (b).

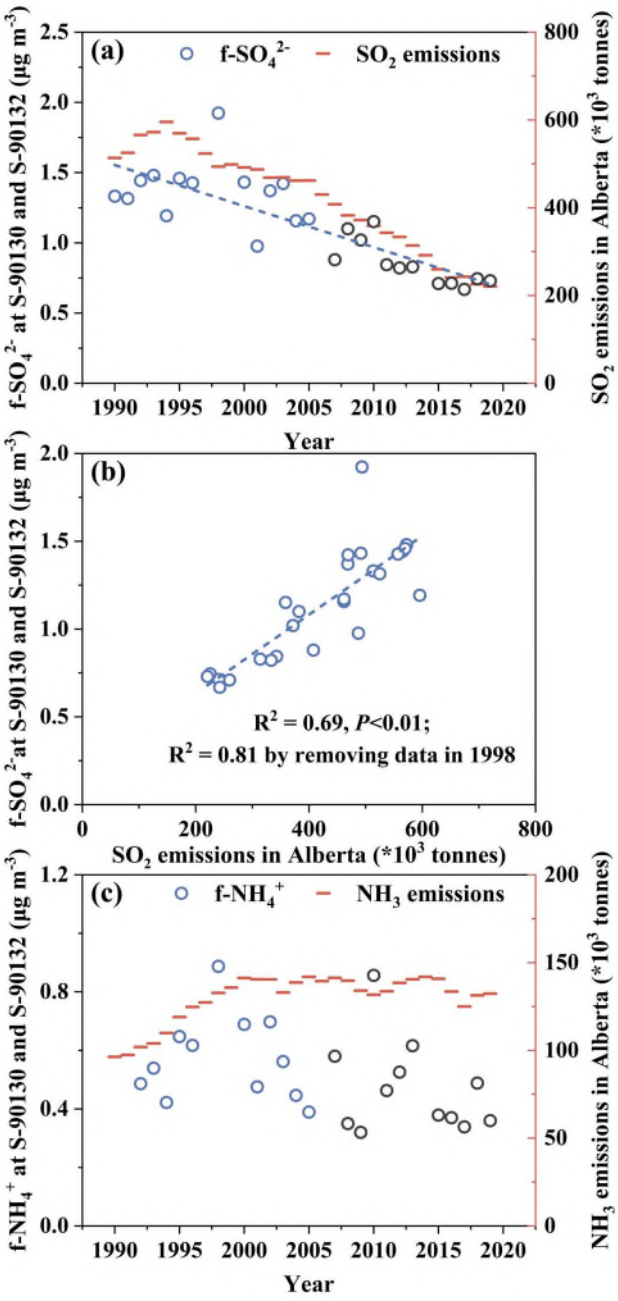

Figure S3. (a) Annual variations of mass concentrations of f-SO_4^{2-} at S-90130 and S-90132 in Edmonton and provincial total SO_2 emissions, (b) f-SO_4^{2-} vs. SO_2 emissions, and (c) same as in (a) except for f-NH_4^+ and NH_3 emissions. Blue and black markers represent the data points obtained at S-90130 and S-90132, respectively.

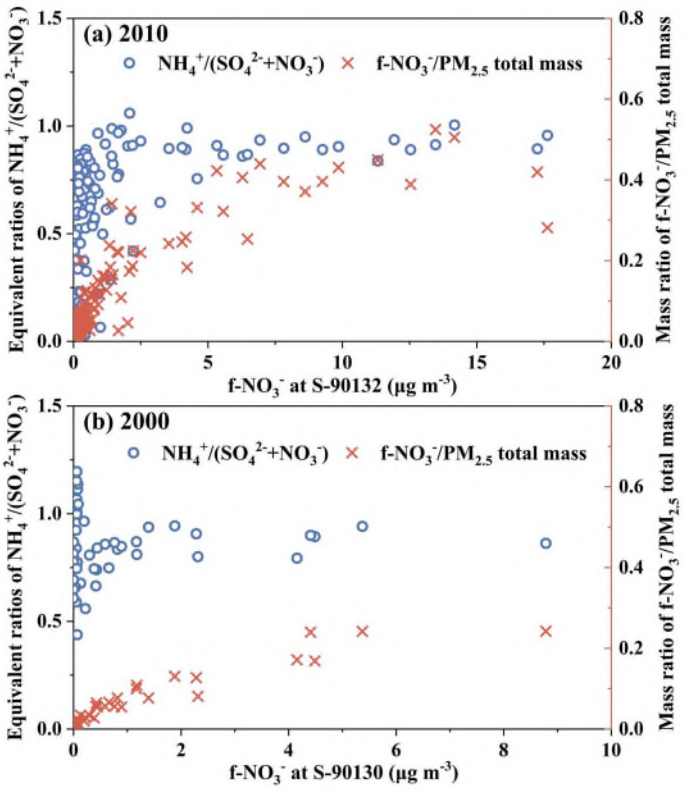

Figure S4. Variations of equivalent ratio of $NH_4^+/(SO_4^{2-}+NO_3^-)$ and mass ratio of f-$NO_3^-/PM_{2.5}$ with f-NO_3^- concentration at S-901932 in Edmonton in 2010 (a) and 2000 (b).

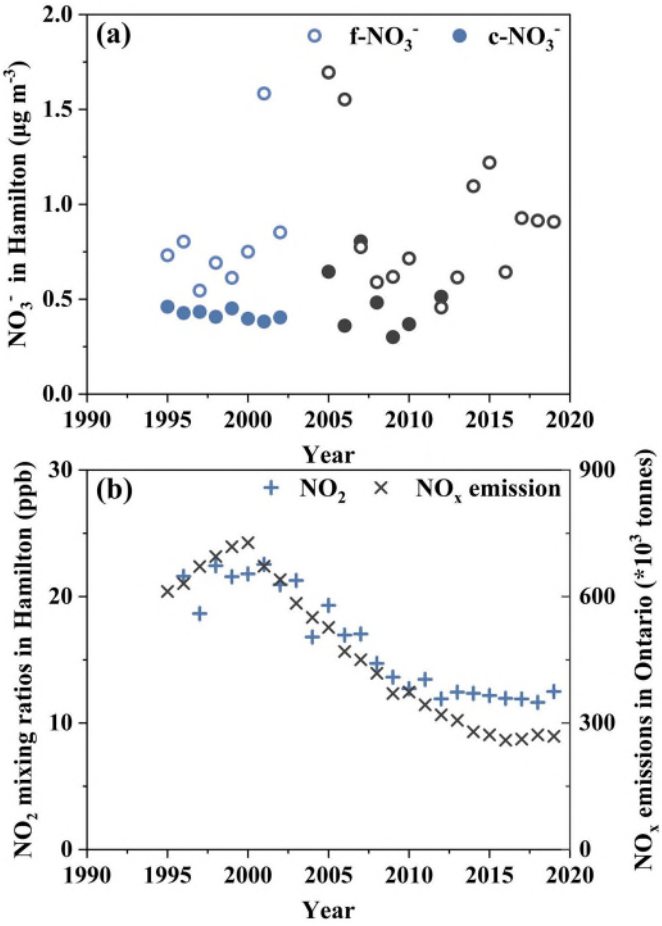

Figure S5. (a) Annual variations of mass concentrations of f-NO_3^- and c-NO_3^- in Hamilton, and (b) annual variations of mixing ratio of NO_2 in Hamilton and provincial total NO_x emissions. Blue and black markers in (a) represent data points before and after 2005, respectively.

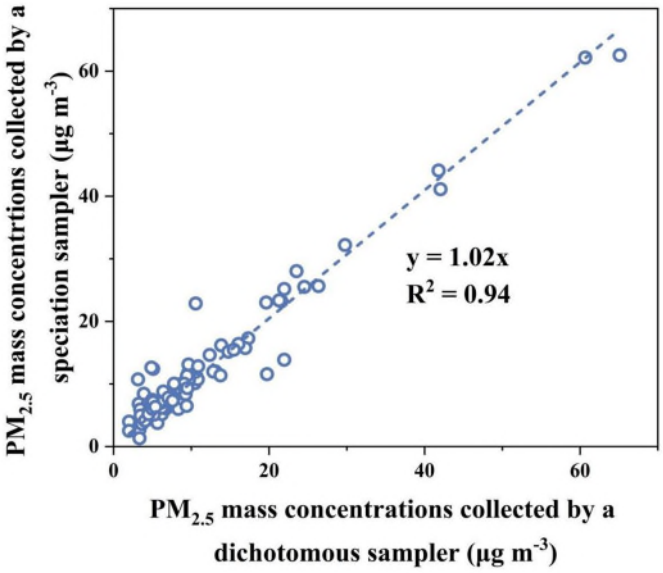

Figure S6. $PM_{2.5}$ mass concentrations measured by a speciation sampler against those measured by a dichotomous sampler at S-90132 in 2010.

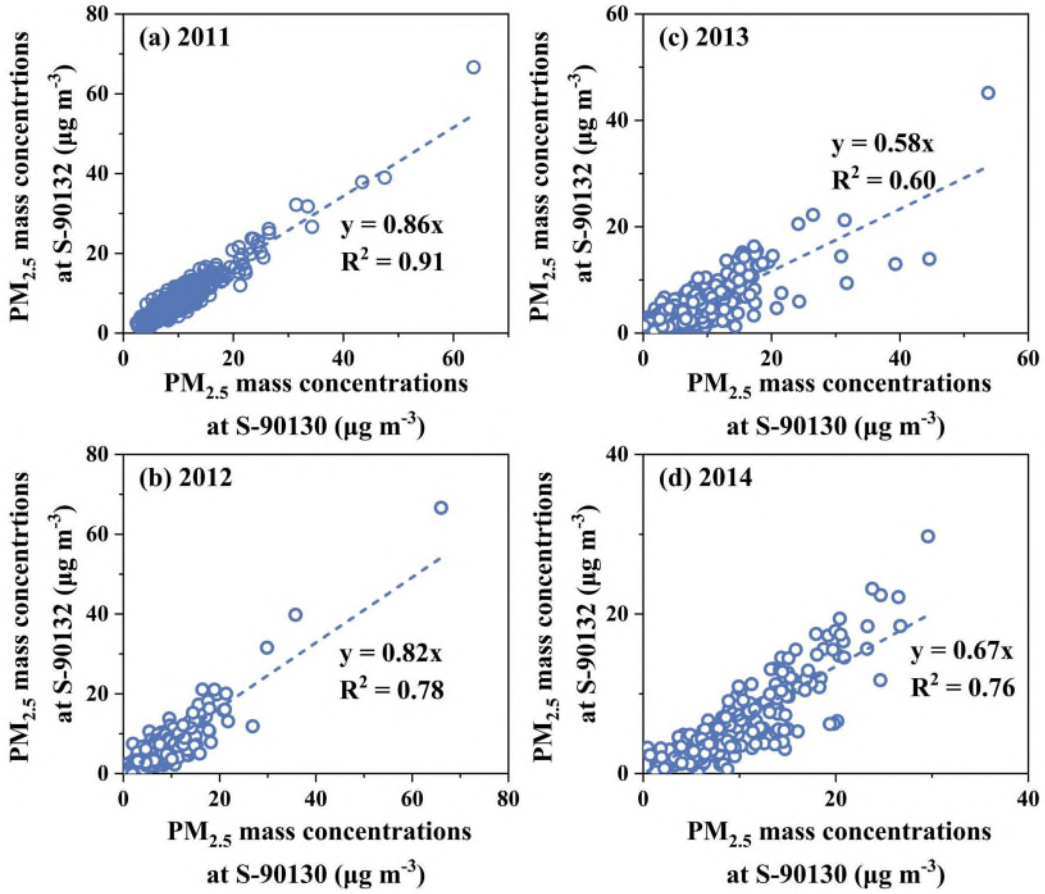

Figure S7. Inter-comparison between real-time measurements of $PM_{2.5}$ mass concentrations simultaneously made at S-90132 and S-90130 in (a) 2011, (b) 2012, (c) 2013, and (d) 2014

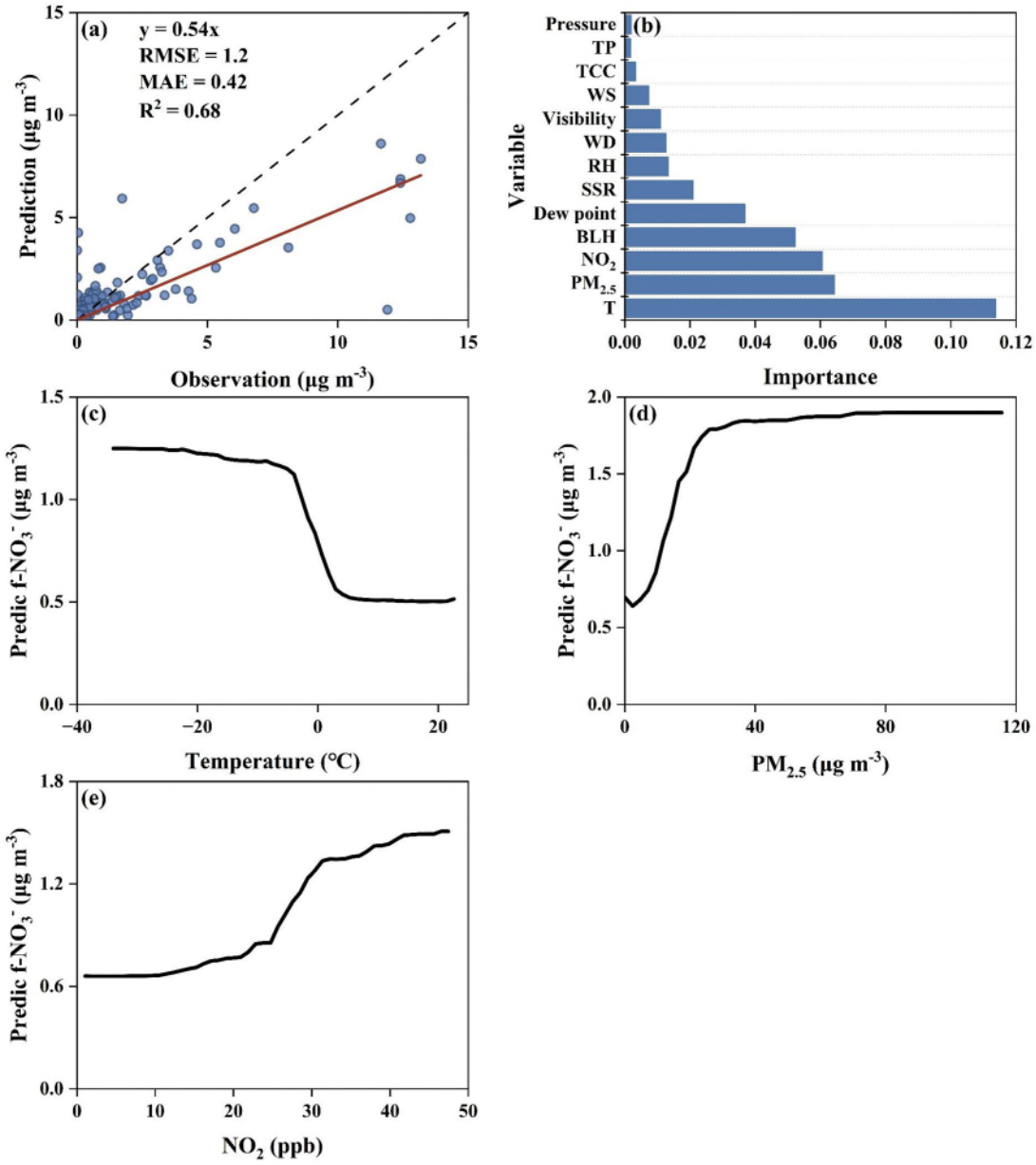

Figure S8. (a) Performance of the Random Forest model for daily f-NO_3^- during 2010–2019, shown as predicted vs. observed values for the 30% test dataset (1:1 line shown; metrics inset); (b) Permutation-based variable importance analysis diagnosing the relative influence of meteorological variables (WS, WD, RH, T, Pressure, Visibility, Dew point, BLH, SSR, TCC, and TP) and chemical species (NO_2 and $PM_{2.5}$) on f-NO_3^- formation; and Partial Dependence Plot of Temperature (c), $PM_{2.5}$ (d) and NO_2 (e).